

Improving Functional Outcomes Through Optimization of Surgical Subdural Hematoma Evacuation Technique

Atishya Ghosh
Uzma Samadani, MD, PhD
Yuk Y. Sham, PhD

1/6/2022

SPECIFIC AIMS Traumatic Brain Injury (TBI) is any alteration in physical, psychological, or neurological status after an impact or force to the head¹. Among other problems, TBI can cause bleeding and clotting of blood on the surface of the brain resulting in subdural hematoma. Untreated, it can become chronic (CSDH) in days to weeks¹. Advancing age and atrophying brain are risk factors for developing CSDH^{1,2,3}. Veterans present a ten-fold higher incidence rate than the civilian population⁴. Expansion of the clot from compression and damage of adjacent brain tissue, can lead to aphasia, stroke, hemiplegia, hemisensory deficits, neurological damage, and death^{1,3}. The one-year mortality rate for CSDH patients is greater than 50% in the elderly 65 years and older¹.

The historical treatment involves surgical drainage using craniotomy which removes a piece of skull > 30 mm or burr hole craniostomy (BHC) which creates an opening of 14 mm in the skull using a high-speed drill¹. Both treatments have a recurrence rate > 10%⁵. A newer, minimally invasive approach called twist drill craniostomy (TDC) makes an incision < 10 mm and can be performed bedside under local anesthesia with decreased length of hospital stay¹. However, TDC suffers from 18% recurrence risk due to imperfect drill placement that results in residual hemorrhage⁵. Recurrence with TDC are hypothesized to be partially due to suboptimal drain placement resulting in incomplete evacuation⁶. This leads to re-accumulation of blood in the subdural space that becomes symptomatic and requires intervention⁷. Non-contrast computed tomography (CT), being more affordable with faster acquisition as compared to MRI, is the imaging modality of choice used for diagnosis of CSDH and monitoring its recurrence post treatment^{1,8}. Historically, surgeons have estimated the incision location for drilling based on viewing of a series of 2D CT images. Typical recommendation places a TDC drain at the thickest site of CSDH for best drainage⁷. However, this practice may be sub-optimal depending on the location, size, shape, and density of the hematoma. A preliminary study by our group using multiple linear regression suggested a drain placed at the anterior end of a hematoma decreases the size of residual hematoma by 56.6% and placing drains at the middle of the hematoma along the craniocaudal axis resulted in 50% more drainage. The regression model with both factors explained 71% of the total drainage. Specific predictors for TDC treatment success from CT images have not been studied vastly. Kolias et al noted that hematomas had different recurrence rates based on density at diagnosis⁹. Other studies have attributed larger preoperative hematoma volume to increased rate of recurrence¹⁰. **Hypothesis:** Understanding the contribution of preoperative characteristics such as hematoma type, size, shape, or density to TDC success rate can support the development of a multivariable regression model to better identify the optimal TDC drill point placement for maximal drainage in neurological surgery planning^{1, 10, 11}. **Scientific Approach:** To accomplish this, a retrospective analysis based on our recently approved IRB of more than 100 pre and post procedure scans of veterans who have undergone TDC evacuation for CSDH will be performed. We will employ unsupervised machine learning to identify CSDH features from a CT scan and supplement it with human guided supervised learning to recognize logical rules that aid in accurate CSDH isolation¹. Additionally, we propose the development of a computational model for TDC drill point placement that enables maximal drainage of CSDH, and a three-dimensional augmented reality neurosurgical planning system for better visualization of patient anatomy to aid a neurosurgeon in placement of the drill.

Aim 1. Develop a segmentation pipeline for CSDH detection from CT scan. Utilizing a hybrid machine learning and supervised learning approach, we will create an automated segmentation pipeline to extract CSDH from a CT based on its location, density, shape, and size. This pipeline will be integrated with Materialise Mimics Innovation Suite v.23.0 to create a 3D computational anatomical model of CSDH.

Aim 2. Develop a machine learning model to predict the optimal drill point placement for maximal drainage of CSDH. We will determine the common threshold for percent of residual hematoma that represents TDC success. We will then develop the next generation regression machine learning models for TDC success patients who had greater versus less successful drainage, for predicting the optimal drill point placement as a function of distance; based on hematoma factors such as location, volume, density, thickness, and shape.

Aim 3. Develop augmented reality for neurosurgical planning for Twist Drill Craniostomy. Using Materialise 3-matic v.15.0, we will optimize the 3D anatomical mesh of the model from Aim 1, for Microsoft HoloLens. We will then create a bedside augmented reality neurosurgical planning system using facial recognition and 3D registration libraries from the augmented reality development software Unity v.2020.1.3f1.

Significance. The proposed study will i) establish a novel chronic subdural hematoma segmentation pipeline ii) improve the success rate of TDC iii) facilitate the implementation of a bedside augmented reality program for neurosurgical procedures. An augmented reality neurosurgical planning system that displays the best position of insertion of the TDC drill for maximal drainage of CSDH, can reduce variability in operator quality and residual hematoma volume post treatment, leading to fewer recurrences and better surgical outcomes.

Abbreviations: traumatic brain injury (TBI), subdural hematoma (SDH), chronic subdural hematoma (CSDH), burr hole craniostomy (BHC), twist-drill craniostomy (TDC), computed tomography (CT), convolutional neural network (CNN)

BACKGROUND & SIGNIFICANCE CSDH is defined as a collection of blood between the lining of the brain-the dura layer, and arachnoid membrane of the brain, often occurring as a result of TBI^{1, 12}. According to the Centers for Disease Control and Prevention, falls are the most common cause of TBI¹³. Frailty is a prevalent condition in the elderly, with up to 60% falling each year and an estimated 30% experiencing multiple falls¹⁴. The CSDH incidence in the United States in 2021 is estimated to be 12.5 % in the elderly population of 65 years and above and, as the population ages, is projected to become the leading indication for cranial procedures for American adults by 2030⁴. At this time, approximately 60,000 CSDH cases are predicted to occur annually in the United States⁴ with 9-79% mortality rate¹.

Age, male sex, trauma, atrophying brain, and antiplatelet and anticoagulant therapy are predominant risk factors for developing CSDH^{1, 16, 17}. Male sex is a confounding variable due to the lack of representation of women in TBI studies¹⁸. Other risk factors include alcohol use, epilepsy, coagulopathy, and cerebrospinal fluid (CSF) shunts, which are rare with clinical presentation^{1, 16}. Brain atrophy can occur after the age of 40, at an increasing rate of approximately 5% per decade¹⁹. The cortical veins between the skull and the brain in the subdural space can experience increased tensile stress from loss of tissue mass. These veins can tear due to tensile stress from severe degeneration of brain and from the allowed greater movement of the brain or due to external forces from traumatic incidents such as falls, resulting in blood accumulating in the subdural space. According to the theory of recurrent bleeding, a fresh bleed or acute hematoma can form an inflammatory membrane around it^{16, 20}. Repeated minor hemorrhages of neovascular structures in the membrane results in hematoma expansion^{16, 21}. The acute hematoma can liquefy to form a chronic subdural hematoma within days^{1, 21}. There may be an increase in the intracranial pressure in the brain from the increased volume¹. The lysis of neutrophils, from an elevated intracranial pressure, releases fibrinolytic products. These products, along with iron and thrombin by-products from heme degradation, can cause the degeneration of brain tissue²². The osmotic theory suggests that the osmotic difference from the fibrinolytic products drives fluid flow into the brain and is hypothesized to be reason for the expansion of the hematoma, although this theory is not widely accepted^{16, 21}. The tearing of the dura from the arachnoid results in the collection of CSF in the subdural space and formation of subdural hygroma. Similar to the membrane surrounding the acute hematoma, the neovascular structures in the membrane encapsulating the hygroma experience repeated minor hemorrhages leading to CSDH^{16, 21}.

A SDH does not always develop immediately. It is often the result of trauma such as falls². A delay of 15-751 days with an average of 49 days can be seen in clinical presentation, as reported by Teale et al. A number of studies report a significant association between anticoagulant and antiplatelet use and bleeding risks leading to the development of CSDH, even in the absence of trauma^{17, 23}. A retrospective study of veteran patients by Samadani et al, in addition to several other studies have found no association between anticoagulant and antiplatelet use and incidence of CSDH in a large veteran population²⁴⁻²⁶. 50-70% of elderly report altered mental status at admission^{1, 2}. Common clinical indications include headaches, blurred vision, vomiting, focal neurological deficits such as hemiparesis, transient neurological deficits such as aphasia, hemiplegia or hemisensory deficits, cerebral ischemia, and seizures^{2, 16, 27}. The characteristics of the hematoma vary depending on the age of the hematoma¹¹. A hematoma between day zero and day seven is hyperdense with the appearance of fresh clotted blood (Figure 1c, left side of scan). The density and appearance and change to more fluid in one to three weeks, a phase known as isodense (Figure 1b). After three weeks, the hematoma density is completely liquefied and is considered hypodense (Figure 1a)^{1, 21}. The hematoma can be further classified based on density into four types- homogenous uniform density, laminar, separated, and trabecular¹¹. Homogenous uniform density indicates a uniform density of hyperdense, isodense, or hypodense throughout. Laminar density has a thin layer of higher density surrounding homogenous contents inside (Figure 1d). Separated has two layers- a lower density layer above the higher density hematoma contents (Figure 1e).

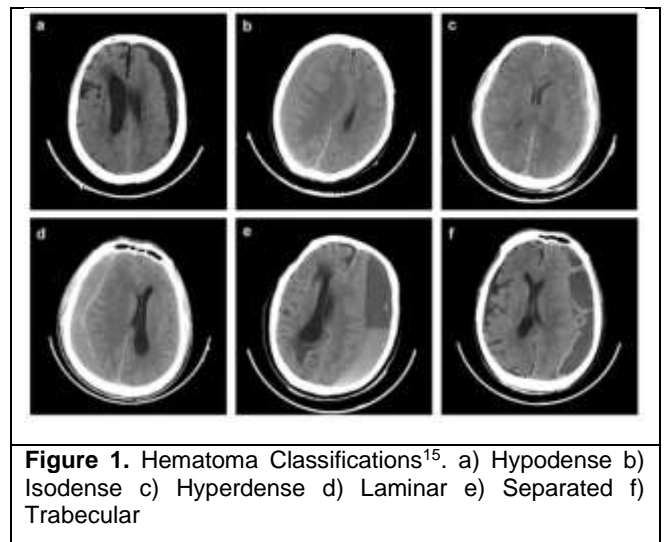
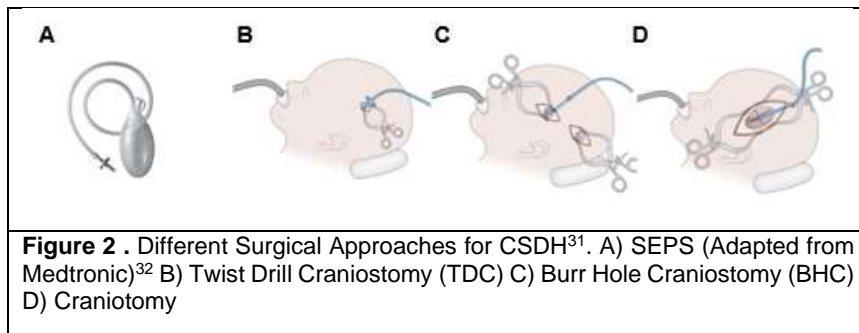


Figure 1. Hematoma Classifications¹⁵. a) Hypodense b) Isodense c) Hyperdense d) Laminar e) Separated f) Trabecular

Laminar and separated are brought about by repeated trauma or rebleeding in the chronic phase. Trabecular is a hematoma marked by a high-density septum arising from fibrosis and new blood vessel formation due to the presence of vascular endothelium derived growth factor (VEGF) in subdural fluid (Figure 1f)^{11, 21}.

Subjective measures such as Glasgow Coma Scale (GCS), a triple-criteria scoring system that measures eye opening, verbal response and motor response, are widely used indicators to gauge the severity of TBI²⁸. Studies have reported that in 62-80% of elderly patients on admission are not suspected to have CSDH before cranial imaging^{2,29}. Non-contrast CT is the imaging modality for CSDH diagnosis as contrast has the same density as blood^{1,30}. Hematomas can be unilateral, appearing on one side of the brain or bilateral appearing on both sides of the brain, with the midline separating the two halves of the brain¹. CSDH has a characteristic crescent shape on a CT scan, particularly in the early phase^{1,2}. Hyperdense hematoma has a more solid consistency and is radiodense, thus appearing brighter than normal brain tissue on the CT scan¹. Hypodense blood clot appears darker on the scan. Isodense hematomas have the same intensity as normal brain tissue, making mid line shift evident on CT an indicator for diagnosis¹. Bilateral isodense SDH is marked by the absence of sulci¹. As CSDH can take weeks to appear due to delayed hematoma expansion, a patient is followed up with repeat CT scanning if initial scan shows no hemorrhage and clinical indications persist²⁹.



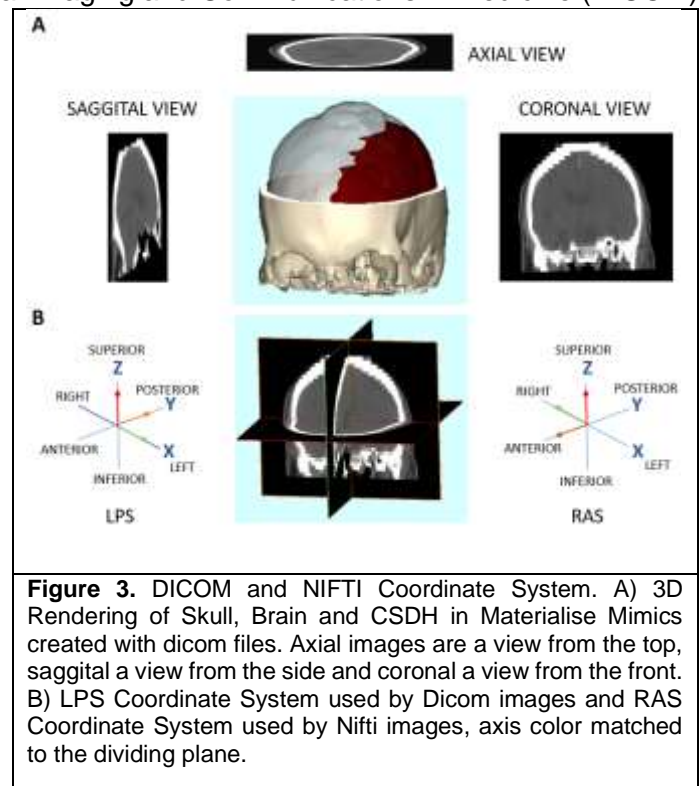
In some patients, a SDH can resolve completely within 4-96 weeks with blood absorption, brain expansion, or clearance with CSF flow^{29, 33}. These patients have a stable neurological status and a smaller hematoma (< 43 ml, thickness < 10 mm, and degree of midline shift < 5 mm)³⁴. For hematomas that have significant mass effect and need evacuation, CSDH can be treated with three surgical approaches-

Craniotomy, BHC and TDC (Figure 2)¹. Craniotomy is performed to evacuate acute CSDH with GCS < 9 or patients with CSDH that have evolved into a solid fibrotic mass or have blood calcification¹. Craniotomy is associated with 0-44% recurrence rate⁵. It is also the preferred treatment choice for recurrent hematomas³⁵. Morbidity from craniotomy is reported to be higher than the drainage procedures BHC and TDC, due to larger opening of the skull⁵. The preferred treatment by most surgeons is BHC, which is performed by creating an opening of 14 mm in the skull after administering general or monitored anesthesia in the operating room to evacuate the hematoma^{1,9}. The location and number of burr holes depends on the size of the hematoma²¹. BHC is often preferred because it allows for easy irrigation of the subdural space³⁶, but holds a higher risk of introducing air into the space which can cause recurrence³⁷. It is associated with 0-28.8% recurrence rate⁵. TDC is similar to BHC but is minimally invasive with < 10 mm opening of the skull and can be performed bedside on a patient under local anesthesia¹. Our study in particular focuses on TDC with SEPS (Subdural Evacuating Port System) which only requires an opening of 5 mm³². TDC leads to less morbidity due to its minimally invasive nature and surpasses the associated risk of cognitive decline with surgery and general anesthesia^{1,38}. However, irrigation during evacuation is difficult with the small opening²¹. TDC is associated with a 3-76% recurrence rate⁵. Drainage for 48-96 hours after TDC and BHC is associated with better outcomes^{5, 21, 39}. Drainage treatments are preferred when the hematoma is liquefied without significantly thick membranes¹. BHC is perceived to have a higher risk of infection due to the introduction of catheter for irrigation and drainage^{1, 21, 40}. SEPS provides an advantage by avoiding the use of catheter for drainage by providing an airtight drainage system to reduce the risk of infection⁴⁰.

Nakaguchi et al reported patients who underwent BHC with frontal drain catheters had 5% recurrence, those with parietal had 38%, with occipital had 36%, and with temporal drains 33%¹¹. This result is similar to our laboratory's preliminary data. Nakaguchi et al also found the highest recurrence rate of 36% in separated hematomas and lowest recurrence rate of 0% in trabecular hematomas versus the homogeneous and laminar types (15% and 19%). They attributed wider subdural space > 10 mm to higher recurrence¹¹. Other studies have reported the pre-operative and post-operative height⁴¹, midline shift¹⁰, preoperative¹⁰ and post-operative hematoma volume³⁷ to be a predictor of recurrence. Some studies report a maximal hematoma thickness > 20 mm to be a predictor of recurrence³⁹, but many studies have not found an association¹⁰. The use of TDC over craniotomy and BHC is suggested, specifically in the elderly, due to decreased perioperative anesthetic complications and better survival outcomes from a minimally invasive procedure^{38, 40, 42, 43}. Accurate placement of TDC requires realistic 3D visualization of the patient anatomy. This can be facilitated by computational

advances in head mounted display devices for augmented reality such as the Microsoft Hololens^{44, 45}. The hololens can project 3D holograms of the skull, brain, hematoma, and optimal drill location onto the real environment with apparent depth and can be aligned to the patient automatically with custom code written in C# integrated with Unity⁴⁶. More optimal placement of bedside TDC could potentially improve drainage, shorten hospitalization, reduce recurrence, and improve cognitive outcomes³. **The central hypothesis of this study is that a computational model developed for placement of drill for twist drill craniostomy, that accounts for location, density, thickness, volume, and shape of a CSDH, while guided by an augmented reality neurosurgical planning system, will enable better hematoma drainage. The proposed neurosurgical planning system developed in this study will enable future clinical research studies to test the hypothesis.** The primary objective of this study is to develop an optimal algorithm for identification of CSDH (Aim 1) and determine the point of maximal drainage (Aim 2), to improve outcomes of TDC surgical treatment. The secondary objective is to create a bedside 3D image-based pre-procedural planning system using augmented reality to visualize patient anatomy and optimal drill location to guide neurosurgeons in the placement of the TDC drill (Aim 3).

RESEARCH APPROACH This study is feasible due to the standard image acquisition procedures adopted by the medical community. CT images are stored in the Digital Imaging and Communications in Medicine (DICOM) digital imaging format⁴⁷. A dicom image consists of two parts – a header and a 2D radiology image, which helps to keep a radiology image connected to the relevant patient⁴⁸. Multiple 2D images constitute a dicom stack. The header includes patient demographics such as name, date of birth and sex⁴⁸. It also consists of CT scanner specifications such as Kilovoltage peak and X ray tube current which can affect the quality of the image through the quality of x-ray and ability to penetrate a patient; and gantry tilt, patient position and patient orientation vector which affects the radiation dose and patient anatomy coordinates⁴⁸⁻⁵⁰. The header also includes scanner image acquisition parameters such as resolution defined by pixel spacing and slice thickness, image dimensions defined by rows and columns, bits allocation for storage and lastly rescale intercept and slope to convert hounsfield values- a measure of radiodensity by linear regression to grayscale intensity values. CT images by default have 512 row pixels and 512 column pixels and dicom images have 16-bit pixel representation^{48, 51}. The dicom images have a coordinate system different from the cartesian coordinate system. The dicom image origin is the center of the first upper left pixel of the image as opposed to the center of the image in cartesian coordinates⁵². Materialise Mimics uses the conventional origin in image processing-the corner instead of center of the first upper left pixel as origin. While loading a dicom stack, the software computes a translation with the pixel spacing attribute in the dicom header to get the required coordinate system⁵².



The human body can be divided by 3 planes. The axial plane divides the body into superior and inferior parts, coronal plane into anterior and posterior parts, and sagittal into right and left parts (Figure 3A)⁵³. CT images are acquired as axial images, which can be reconstructed to form the sagittal and coronal views⁵⁴. Dicom images and Mimics use the LPS (Left, Posterior, Superior) anatomical coordinate system (Figure 3B). The X-axis is increasing towards the left side of the patient, the Y-axis towards the posterior side and the Z-axis towards the head of the patient⁵². The dicom format is widely used for analysis because all CT scanners use the format and it is the conventional format to store in any hospital's PACS (Picture Archiving and Communication System) server, the system for storage, transmission, and retrieval of radiology images⁵⁵. The dicoms contain patient identifiers and need to be de-identified prior to analysis using an opensource python library pydicom v.2.2.2⁵⁶. Another file format preferred for analysis is the Nifti file format as it does not store patient PHI in its metadata like a dicom header⁵⁷. Nifti file format differs from the dicom by being a single file representing a 3D volume, while dicom format consists of multiple 2D files to construct a 3D volume⁵⁷. The Nifti file format uses the RAS

coordinate system (Right, Anterior, Superior) with the origin as center of the 3D stack on the anterior commissure⁵⁷ (Figure 3B). The LPS or the RAS coordinate system can be converted to the world coordinate system by an affine transformation using the voxel size. The rotation and translation matrix elements for the affine transformation vary for the two formats by a negative sign. Most image processing softwares can compute these transformations automatically but when using multiple file formats for algorithmic development in python, it is important to ensure coordinates are in the same space⁵⁷.

Isolation of an anatomy using extracted features such as intensity or texture from a biomedical image is called segmentation⁵⁸. There are supervised and unsupervised methods for segmentation. Unsupervised methods use graphical models or clustering algorithms such as Expectation Maximization (EM), K-Means or Hierarchical clustering on unlabeled data for the task⁵⁹. Supervised learning uses prior knowledge for an image processing task while training samples^{58, 59}. Some examples include CNN, support vector segmentation, random forest and K-nearest neighbor segmentation methods⁵⁸. We employed K-Means clustering and leveraged domain knowledge of the data through better understanding of the disease from a neurosurgical perspective, to create rules (Aim 1.2) for segmenting the hematoma from our scans⁶⁰⁻⁶². This approach of applying domain knowledge to improve segmentation has been successful in segmentation of liver from low contrast CT images⁶⁰, neurons and astrocytes from Electron Microscopy (EM) Images⁶³, mitochondria from EM data⁶⁴ and anatomical structures from cardiac MRI⁶⁵.

The Kmeans algorithm initializes k centroids for k disjoint clusters^{60, 66}. The objective of the algorithm is to cluster every gray scale intensity value into the cluster with the minimum euclidean distance. After every sample is assigned a cluster, the centroids or average value of every cluster are updated. Every point is reassigned a cluster based on the minimum euclidean distance. The algorithm converges after a finite number of iterations when the clusters no longer update^{60, 66}. The algorithm can be mathematically represented for the 2 steps as,

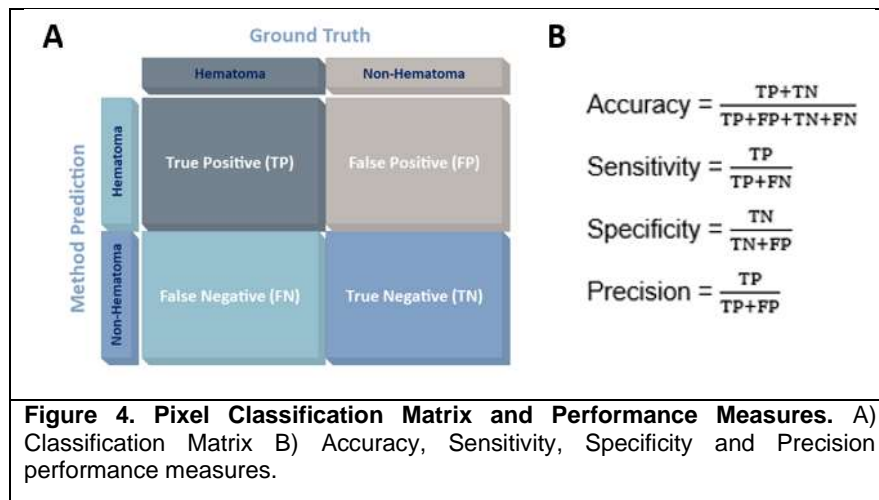
Step 1 : $z_q \rightarrow C_i$ if $\|z_q - m_i\|^2 < \|z_q - m_j\|^2$, where m_i is the initial set of means with i ranging from 1 to k, j ranges from 1 to k but $j \neq i$, z_q is an arbitrary pixel intensity value with q ranging from 1 to 262,144 and C_i represents disjoint cluster sets with i ranging from 1 to k.

Step 2 : $m_i = \frac{1}{|C_i|} \sum_{z \in C_i} z$, where $i = 1, 2, \dots, k$ and $|C_i|$ is the number of samples in cluster i

The first step represents the initialization of the algorithm by specifying an initial set of means, followed by the assignment of every pixel intensity value to the nearest cluster based on minimum euclidean distance. Step 2 represents an update of the cluster means⁶⁶.

Current algorithms for subdural hematoma segmentation utilize neural network, specifically CNN. Blast CT is a software designed for cranial hemorrhage segmentation⁶⁷. The software uses the popular Deep Medic model which is a 3D CNN specifically created for brain lesions⁶⁸. Deep Medic is a supervised learning network with 11 layers and parallel convolutional pathways that process images at 2 scales- a normal resolution and a lower resolution to learn more features and to keep the computational cost low. The network employs batch normalization to ensure same input size at every layer to increase the speed of training and residual networks to reduce vanishing gradients for faster training by preventing slow weight updates and learning identity functions better^{66, 68}. The deep medic network is trained on the BRATS database containing MRI of patients with glioma⁶⁸. Blast CT adopts the architecture and trains 2 independent datasets containing 98 CT scans and 839 CT scans of cranial hemorrhages⁶⁷. Blast CT is initially trained for 1200 epochs with an initial learning rate of 0.001, that is halved every couple hundred epochs⁶⁷. It uses cross entropy loss function to penalize a lower probability of a class prediction for a pixel significantly more using negative log of the probability to enable accurate prediction after training⁶⁹. The adaptive gradient optimizer RMSProp is used for faster training being a modified gradient descent algorithm with a momentum parameter, reducing oscillations to reach label while training⁷⁰. It augments the data with flipping, intensity deformation and elastic deformation to reflect a wide range of scans. Every epoch uses 50 images with a patch size of 110*110*110 mm⁶⁷. Blast CT has a robust training whose performance was validated on 490 patients from the CQ500 dataset containing different cranial hemorrhages including chronic subdural hematoma⁶⁷. The performance of our pipeline is compared with Blast CT in our study. Another architecture that is used extensively in the biomedical field is the UNET CNN⁷¹. The architecture is U shaped and has a contraction and an expansion path. The contracting path consists of two convolution layers with 32 and 64 3*3 filters with ReLu activation function and two max pooling layers with 2*2 filter. The goal of the contracting path is to learn the features in an image⁷¹. Since convolution reduces the size of the image, the expanding path consists of up-sampling convolutional layers with ReLu activation and max pooling layers to get

the segmentation map in the original space with transposed convolution⁷¹. The expanding path also concatenates high level features at each layer from the contracting path^{71, 72}. The ReLu activation returns 0 for output map if the result of a function at a neuron during training is negative and keeps the positive value if the result is positive⁷³. This results in faster training as the derivative of the function with respect to the input results in larger weight updates than other functions such the sigmoid function⁷³. UNET was specifically created for biomedical images to segment glioblastoma and astrocytoma from thirty EM images. It was created to achieve high segmentation accuracy with less training data on low contrast images and on anatomical structures with weak outer borders and stronger inner borders⁷¹. UNET gives the background boundary pixels between neighboring structures and outer boundaries a bigger weight for the loss function, to achieve higher accuracy in segmentation⁷¹. It has been used to delineate cisterns in head CT scans by Jain et al and kidneys and kidney tumors by Zhao et al^{72, 74}. The performance of our pipeline is compared to the implementation of UNET in dragonfly software version 2020.2.0 build 941.



non-hematoma and False Negative (FN) if the true label is hematoma but the algorithmic prediction is non-hematoma (Figure 4A)⁷⁴. The performance measures are calculated by formulas in Figure 4B^{72, 74}. Accuracy gives a value for general segmentation performance of algorithm on both classes, precision denotes the fraction of true positives out of all positive predictions, sensitivity is a measure of the proportion of hematoma pixels that are correctly detected, and specificity demarks the proportion of non-hematoma pixels that are correctly detected⁷⁵.

Resources: The data for the study is collected from the Minneapolis and New York VA hospital database. Data collection is facilitated by a windows laptop provided by the Minneapolis VAMC. All analysis will be done in python⁷⁶ utilizing Samadani and Sham lab workstation resources. The Samadani lab provides a windows workstation and the microsoft hololens, and Sham lab a linux environment in addition to access to the Materialise Mimics Innovation suite v 23.0 and Materialise 3-Matic v.15.0 through the Minnesota Supercomputing Institute (MSI). Dragonfly version 2020.2.0 build 941 is run on the windows workstation with an academic license. The ground truth segmentation is done using ImageJ version 1.8.0_172. Unity Long term Support (LTS) version 2019.4.11f1 is run on the windows workstation with a developer license to create an augmented reality application. Visual Studio 2019 is used for deploying an application to the hololens.

Aim 1. Develop a segmentation pipeline for CSDH detection from CT scan.

(✓) **Aim 1.1. Develop an IRB protocol to collect a dataset of >100 patients with CSDH who have undergone SEPS TDC.**

Rationale: We propose. **Approach:** An IRB protocol has been developed for a retrospective study of at least hundred subjects who underwent TDC subdural evacuation with SEPS in the VA database VINCI. Pertinent CPT codes 61154 and 61156 were used to identify a patient cohort who have undergone drainage for CSDH between the years January 1, 2005 and March 1, 2019 at a VA hospital nationally, with a SQL Query executed in Microsoft SQL Query Management Studio v17.0. A second SQL query is used to create a table with patient last name, date of birth, patient ID, social security number (SSN) and accession numbers of CT images of CSDH patients at the Minneapolis VA Medical Center (VAMC) and New York Harbor HealthCare System (NYHHS), from the initial patient cohort.

This information is needed to acquire radiographic images. The query is built with the inner join function connecting different tables in the VINCI database with the required information using primary keys such as patient SSN or patient ID. The images of patients treated at the Minneapolis VA Medical Center (VAMC) are acquired through their PACS server Visage 7.0. Since this is a multi-site study involving the New York Harbor HealthCare System (NYHHS), images of patients treated at NYHHS are transferred from the New York PACS server Phillips Intellispace Radiology to Minneapolis PACS Visage 7.0. The CT scans for each patient are downloaded from Visage, deidentified adhering to HIPAA regulations, and sorted by acquisition date in the dicom header for analysis with a custom python script created using python libraries pydicom and os^{56, 76, 77}. A cross-table spreadsheet linking the identifiers to the de-identifiers is created with the same script. The CT scans retrieved is stored in the Neurotrauma research drive at the Minneapolis VA, behind the VA firewall. The data is transferred to the University of Minnesota for analysis using a VA encrypted ironkey.

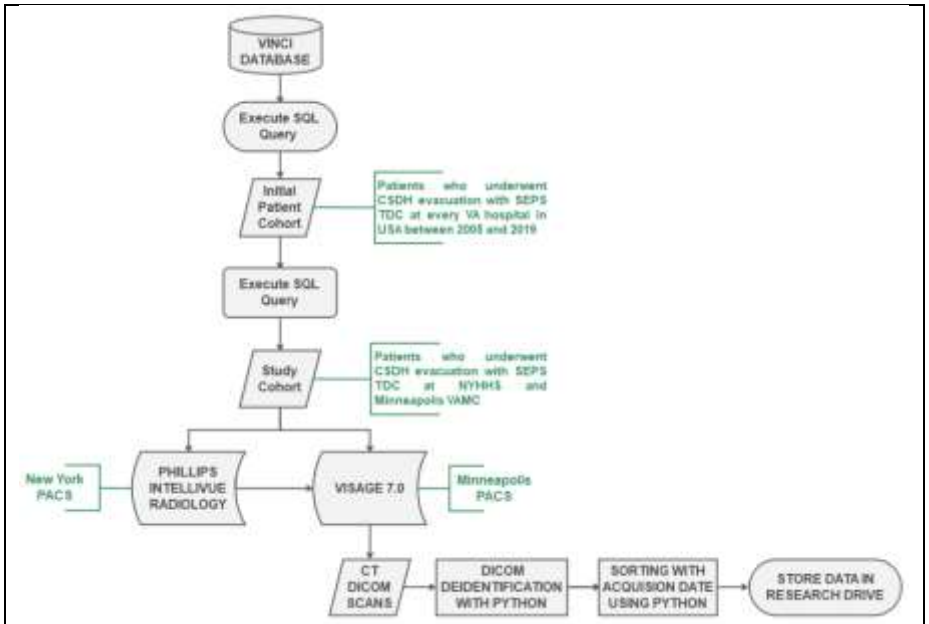


Figure 5. Flowchart depicting CT Image Acquisition from VINCI Database. The flowchart highlights the process to acquire head CT scans of patients who underwent TDC evacuation with SEPS at Minneapolis VAMC and NYHHS from the VA database VINCI.

(✓) Aim 1.2. Develop an automated 2D segmentation pipeline for CSDH.

Rationale: Since a hematoma has several classifications based on appearance and CSDH is a later stage, we reduced the scope our problem to hypodense hematoma for preliminary analysis. We started with open-source algorithm Blast CT to segment the hematoma. Blast CT segmentation with its pretrained models did not achieve the accuracy we require for our study. We implemented the UNET convolutional neural network in dragonfly and achieved a moderately successful segmentation. We develop our pipeline with the Kmeans algorithm and image processing techniques such as intensity thresholding and region growing. **Approach:** As a preprocessing step, we utilized a UNET convolutional neural network to denoise our images⁶⁶. The Kmeans algorithm clusters an image using gray value intensity ranging from 0 – 255^{60, 66, 78}. The number of clusters was chosen to be 7 based on the elbow method using inertia and supervised learning on our training set of 28 images (80-20 train test split of total available 35 patients). The elbow method suggests the optimal cluster is where inertia - the sum of squared distances of samples to their closest cluster center stabilizes (Figure 6A)⁶⁶. With Kmeans, pixels with value 0 get clustered as background, 255 as skull and the remaining clusters include different anatomical structures such as ventricles and radiographic presentations such as subdural hematoma. The hematoma cluster after the implementation of Kmeans algorithm is selected with intensity thresholding^{66, 79} rule that states the

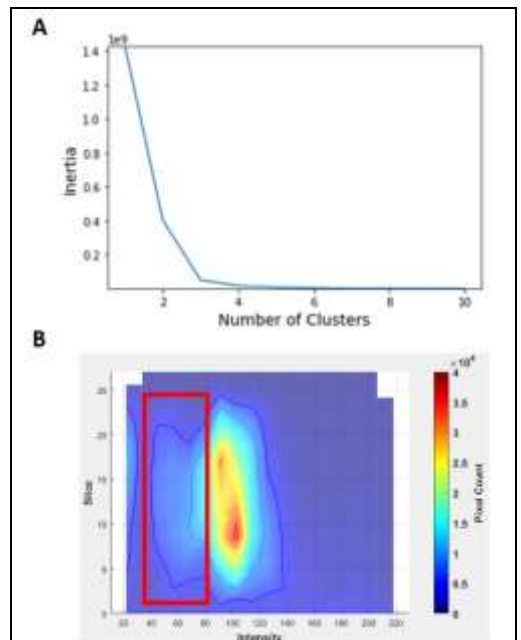


Figure 6. Kmeans and Intensity Thresholding Parameterization. A) Kmeans Inertia stabilizes at 5 clusters B) Intensity and Pixel Count of hypodense hematoma

Kmeans centroid of the cluster should belong to [45, 105], based on contour plot indicating the intensity range for a hypodense hematoma (Figure 6B).

Supervised learning confirmed this range to pick the hematoma cluster on 27 other images. The hematoma cluster at this step contains the hematoma in addition to several other noisy connected clusters. Region Growing algorithm is implemented to segment all the connected components^{66, 79}. Since most region growing algorithms require a manual initial start point to start the algorithm, a modified region growing algorithm was implemented to keep the pipeline automated⁶⁶. We employ data structure stack that allows for a particular order in which the operations are performed on the elements in the stack⁸⁰. The first element that goes into the stack, leaves the stack for the operation to be performed⁸⁰. The script starts at the top left pixel of an image and initiates the modified region algorithm by assigning a pixel to the stack if it is not the background pixel and has a non-zero value⁶⁶. This pixel is given a label 1. The neighboring pixels of this pixel are evaluated and added to stack if they meet the following conditions : a) are not background pixels b) they haven't been given an integer label and c) the pixels lie within the bounds of the image. If the conditions are met, the pixels are given the label 1. If not, the algorithm exits of the while loop and continues inspecting pixels in the index range for the initial condition to find the next seed. The algorithm iteratively increases the integer value for the label for each connected component. The output of this algorithm is an image where every pixel of a connected component has a specific integer value⁶⁶. This output is the input to the next three steps in the pipeline: 1) pixel thresholding 2) distance to center of skull thresholding 3) distance to skull thresholding. Domain knowledge such as the mass effect of a CSDH and the proximity of the CSDH to the skull being a surface bleed was used to create the above-mentioned thresholding rules^{62, 63}. Supervised learning with 28 images was used to identify the threshold values. A connected component was considered to be a hematoma if its : 1) Area > 800 pixels (Figure 6B) 2) Euclidean distance of centroid of component from center of the skull > 72 pixels 3) Euclidean distance of the nearest pixel of the component to the skull < 7 pixels. The final output after the implementation of our pipeline is an image with the segmented hematoma.

To reduce the computational cost of calculating the distance between every pixel of the hematoma and every point on the skull, the image is divided into quadrants and analysis is restricted to quadrants. Only the distances between hematoma and the skull pixels in each quadrant was calculated. The minimum distance for hematoma pixel to the skull for each quadrant was collected and further the minimum of the four values was considered to be the closest distance to the skull. Another anatomical feature near to the skull that has the same characteristics such as intensity as the hematoma is gyri. We train a UNET convolutional neural network to extract the gyri and subtract the gyri pixels from the output of the thresholding steps⁷¹. This is the final step that gives us our hematoma segment. Figure 7 represents the entire workflow. **Data Analysis and Interpretation:** We

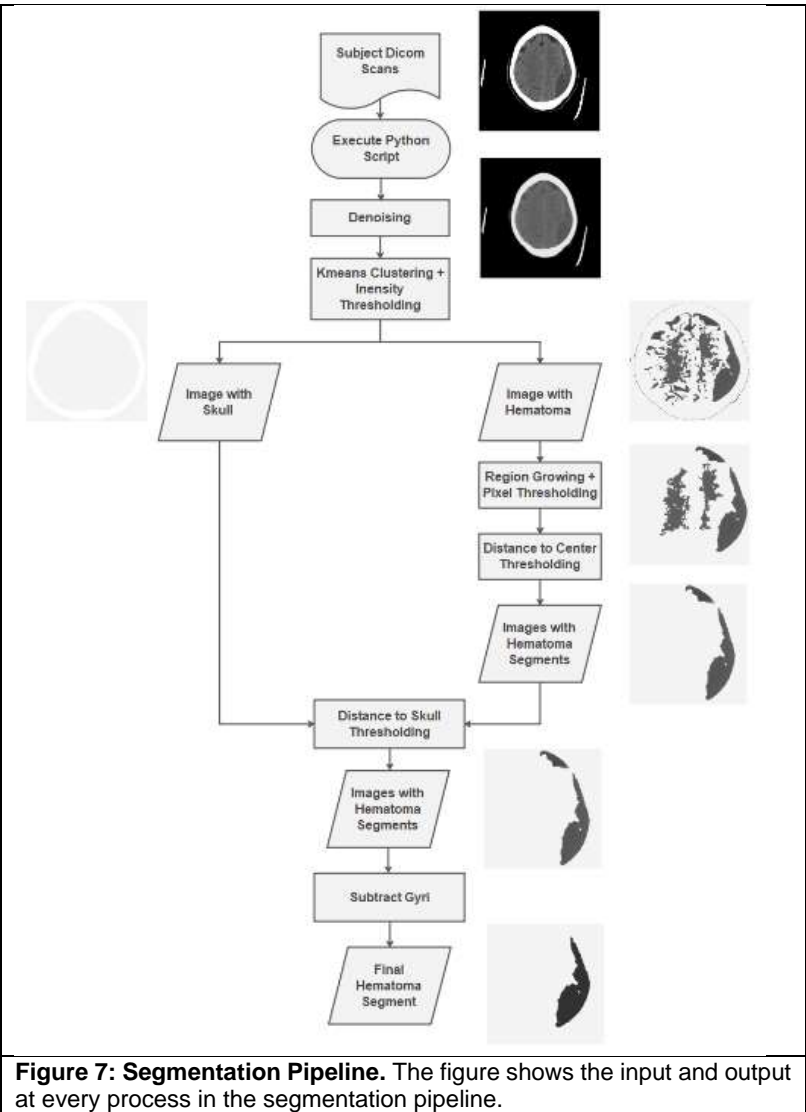


Figure 7: Segmentation Pipeline. The figure shows the input and output at every process in the segmentation pipeline.

Measure	UNET	Blast CT	Pipeline
Accuracy	97.99	97.60	97.83
Precision	65.19	20.29	63.79
1-Specificity	0.010	0.001	0.012
Sensitivity	56.22	3.09	62.52

Figure 8. Performance Comparison. 1-Specificity and Sensitivity is highest for our segmentation pipeline.

Figure 8. Performance Comparison. 1-Specificity and Sensitivity is highest for our segmentation pipeline.

compared the segmentation results at pixel level for all 3 methods as described in research approach. Our pipeline performs moderately better than the other two methods (Figure 8).

(✓) **Aim 1.3. Construct a 3D model of CSDH and compute its volume.**

Rationale: In this aim, the segmentation output from Aim 1.2 is used to construct a 3D volume of the CSDH in Materialise Mimics v.23.0 using an adaptive marching cubes algorithm⁸¹. **Approach:** The marching cubes algorithm creates a triangle mesh by iterating over a uniform grid of cubes to fit the function $f(x,y,z) = 0$ ⁸¹. Based on the location of vertices of each cube, a triangle mesh is generated with fifteen unique possibilities⁸¹. Given that volumetric construction with Materialise Mimics has been used for clinical applications such as separation of Thoraco-Omphalopagus conjoined twins⁸² and bone reconstruction for hip arthroplasty⁸³, we trust the construction algorithm in Mimics (Figure 9). **Data Analysis and Interpretation:** We also validated the software constructed volume with 3D manual segmentation of a hematoma for one patient. The volume of the manual 3D segmentation was calculated using the formula below⁸⁴.

$V = t \sum_{i=1}^n A_i$, where V = Total volume, n = number of slices in a dicom stack, A_i = Area of the segmented hematoma for slice i and t = slice thickness which is a constant number across a 3D Dicom stack. The volume between the software construction and manual computation differs by 4 ml. The difference can be attributed to inaccuracy in manual segmentation around edges and inclusion of isodense pixels within the hematoma, which the pipeline output does not include.

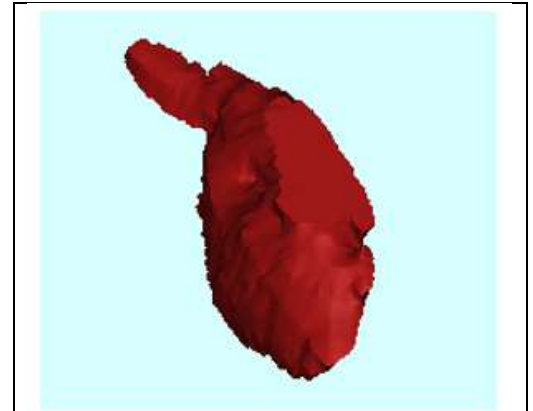


Figure 9. 3D Construction of Hematoma. Adaptive marching cubes algorithm is used to construct a 3D model of hematoma from 2D segmentation output in Aim 1.2 in Materialise Mimics.

Aim 1 pitfalls and alternative strategies: Aim 1.3 is dependent on completion of aim 1.2. Given the large number of patients we are trying to analyze, we aim to improve the automated segmentation methods by expanding the UNET to a 3D UNET⁷⁴, retraining blast CT⁶⁷ or refining our pipeline with automated contrast enhancement and including other domain features such as midline shift^{72, 85}. As we have demonstrated, aim 1.3 is feasible with manual segmentation. The expected outcome from aim 1 is a 3D segmented model of CSDH from a head CT scan.

Aim 2. Develop a machine learning model to predict the optimal drill point for maximal drainage of CSDH.

(✓) **Aim 2.1. Determine CSDH characteristics volume, surface area, density, thickness, and shape from Head CT scan.**

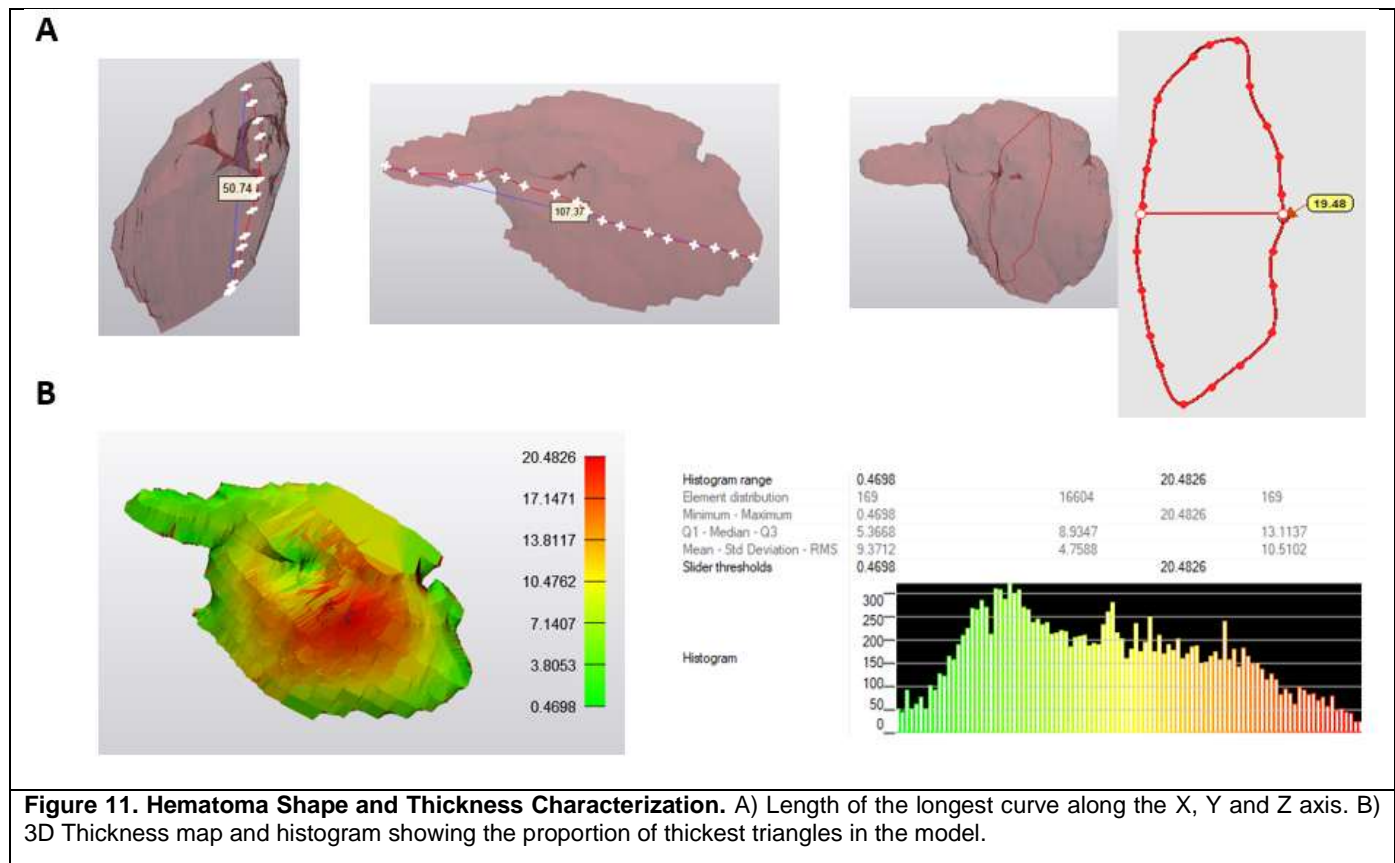
Rationale: In this aim, we characterize the CSDH with quantifiable variables. We construct a 3D model as in Aim 1.3 for the CSDH pre surgery and compute its volume. We use custom scripts to access specific modules in Materialise Mimics and 3-Matic to determine the density, shape characteristics which include longest fitting curve along the X-axis, Y-axis, Z-axis, maximum, median, and average thickness, and surface area of the CSDH. **Approach:** Mimics has a module to compute the average density, volume, and surface area using Finite Element Analysis (FEA)⁵². It is difficult to compute these measurements for a complex geometry. FEA generates a volumetric mesh for a 3D object and solves the governing equations for a parameter in smaller domains and then couples the analysis over the entire object to provide an estimate that matches experimental measurements⁸⁶. We also calculate the

FEATURE	MEASURE	UNITS
Volume	42738.92	mm ³
Surface Area	9267.85	mm ²
Surface Area/Volume	0.22	mm ⁻¹
Average Density	34.8	Hu
Maximum Thickness	20.48	mm
Median Thickness	8.93	mm
Average Thickness	4.76	mm
Maximum length (X)	50.74	mm
Maximum length (Y)	107.37	mm
Maximum length (Z)	19.48	mm

Figure 10. CSDH Characteristic Features. The figure shows the different characteristics to describe a hematoma.

ratio of surface area to volume to account for the complexity and variation in hematoma geometry⁸⁷. These features are computed for the CSDH in Figure 10. The shape is characterized with the length of the longest fitting curve along the X, Y and Z-axis (Figure 11A). We are currently using the curve length feature from the measure module in 3-Matic to manually identify the curves while we develop a method such as an ellipsoid fit to

quantify these lengths automatically⁸⁸. Figure 11 B shows a 3D thickness map of the CSDH and histogram showing the distribution of thickness values. The dark red region in the center is the thickest. **Data Analysis and Interpretation:** Two triangles in a FEA mesh are considered to be opposite if the angle between their normals is greater than 120°. 3-Matic uses the distance to the closest opposite triangle to assign a thickness. The automatic meshing can result in opposite triangles around the edges, producing inaccuracy in thickness measurements at the boundary⁸⁹. We plan to remesh the CSDH object by using the adaptive remesh feature in 3-Matic to reduce this error in the future.



() Aim 2.2. Develop a machine learning model to predict the optimal drill point for maximal drainage of CSDH. Rationale: We characterized the CSDH, and residual volume at 48 hours, 6 months, and 9 months post SEPS TDC using the features in aim 2.1 for 2 patients. (Figure 12). The first patient had no recurrence and the second showed recurrence at 3 months and underwent another TDC.

PATIENT 1

FEATURES	Vol (mm ³)	SA (mm ²)	SA/Vol (mm ⁻¹)	RD (Hu)	Max Thic (mm)	Avg Thic (mm)	Median Thic (mm)	Max Len X (mm)	Max Len Y (mm)	Max Len Z (mm)
PRE TDC	113183.79	26075.18	0.23	47.72	17.39	8.39	8.3	147.89	174.72	18.33
POST TDC (48 hours)	77087.48	21872.66	0.28	42.36	14.54	6.85	7	101.68	173.69	14.27
Δ _{48 hours}	36096.31	4202.52	0.05	5.36	2.85	1.54	1.3	46.21	1.03	4.06
POST TDC (3 months)	14275.23	5390.74	0.38	31.5	12.29	5.84	5.96	33.68	63.2	13.49
Δ _{3 months}	98908.56	20684.44	0.15	16.22	5.1	2.55	2.34	114.21	111.52	4.84
POST TDC (6 months)	11980.44	4690.69	0.39	37.3	11.93	5.11	5.37	29.89	59.37	13.73
Δ _{6 months}	101203.35	21384.49	0.16	10.42	5.46	3.28	2.93	118	115.35	4.6
POST TDC (9 months)	NO SCAN									
Δ _{9 months}	NA									

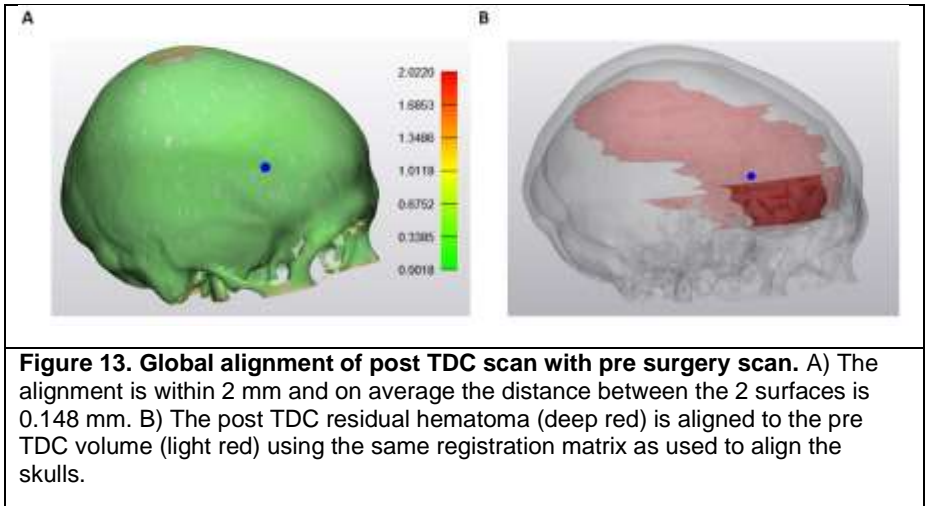
PATIENT 2

FEATURES	Vol (mm ³)	SA (mm ²)	SA/Vol (mm ⁻¹)	RD (Hu)	Max Thic (mm)	Avg Thic (mm)	Median Thic (mm)	Max Len X (mm)	Max Len Y (mm)	Max Len Z (mm)
PRE TDC	56392.94	19749.52	0.35	52.06	12.35	5.92	5.07	69.42	190.77	12.37
POST TDC (48 hours)	42776.22	19005.99	0.44	40.35	8.82	4.6	4.73	57.94	142.06	9.28
Δ _{48 hours}	13616.72	743.53	0.09	11.71	3.53	1.32	0.34	11.48	48.71	3.09
Recurrent (3 months)	59727.61	19539.15	0.33	56.83	11.91	5.97	6.24	102.86	168.6	10.95
POST TDC (48 hours)	50822.21	18851.19	0.37	59.59	12.26	5.69	5.68	60.69	177.66	12.81
Δ _{3 months}	8905.4	687.96	0.043786597	2.76	0.35	0.28	0.56	42.17	9.06	1.86
POST TDC (6 months)	NO SCAN									
Δ _{6 months}	NA									
POST TDC (9 months)	0									
Δ _{9 months}	NA									

Figure 12. CSDH FEATURES. Change (Δ) is measured with respect to most recent TDC diagnosis.

Figure 12 shows the CSDH features pre TDC and residual volume features post TDC. The change in variables is measured with respect to pre TDC values for patient 1. Since patient 2 had recurrence, change at the 3 months was quantified with respect to the recurrent hematoma. A regression model to predict the optimal drill point as a function of distance for maximal drainage of CSDH will be created using the residual hematoma volume and hematoma characterizing variables.

Approach: Post TDC patient anatomy is aligned to initial spatial anatomy to annotate the drill point with regards to pre- treatment scan with global registration in 3-matic. Global registration minimizes the euclidean distance between points on two 3D surfaces for alignment⁸⁹. The alignment of the post and pre skull is within 2 mm and the average distance is 0.148 mm (Figure 13A). The registration matrix to align the skulls is used to align the residual hematoma post TDC to the original hematoma. The blue dot marks the drill point. The preliminary study by our research



group developed a multiple linear regression model that identifies a relationship between drill placement location with respect to size of the hematoma and residual hematoma. The location of drill was marked as a function of distance along the length of the hematoma on the anteroposterior axis and cranio-caudal axis. The study notes that TDC drill placed at the center of a hematoma and anterior end of a hematoma resulted in better drainage compared to placement at the centroid of the hematoma. The study variables were restricted to the shape of the hematoma to avoid overfitting the data. After validation with shape, we will iteratively add to the model variables from aim 2.1⁷⁵. In addition, we will test if the drill location at the center of mass weighted by intensity results in better drainage. **Data Analysis and Interpretation:** The preliminary study by Samadani et al will be repeated as such with a larger number of patients to validate the results. The relationship of each variable with residual volume will be tested independently using pearson coefficient as a measure. Only the variables that are strongly correlated to residual volume will be added as variables to the multiple regression model⁷⁵. Variables will be grouped to improve the performance metrics of the model⁷⁵. We will also test the performance of other supervised learning models such as lasso, ridge regression and random forest regression. Lasso algorithm reduces the irrelevant features while identifying a linear relationship between multiple features and the output variable⁵⁹. Random forest regression also helps with feature reduction by listing the importance of each feature as a numerical value for prediction. It builds multiple decision trees based on training data. Each tree predicts the output variable and an average of all the predictions is the output of the algorithm⁹⁰. Ridge regression is beneficial for multiple regression when several variables are correlated⁵⁹. Given the wide range of hematoma characteristics, to avoid generalizing a model, we can also build separate models for optimal drill location based on specific hematoma characteristics such as size and density.

Aim 2 Pitfalls and Alternate Strategies: There might not be a sufficient number of patients who had pre- and post-drainage CT scans for SEPS TDC procedure at the engaged VA sites. In this case, we will develop additional collaborations with other VA sites. We assume that the majority of TDC failures could be eliminated with better drain placement. However, it is conceivable that TDC fails for other reasons such as failure to penetrate membranes during drain placement or septum formation of the CSDH. In that case, this aim can help to identify radiographically those patients whose CSDHs are not amenable to craniostomy and will require craniotomy. As demonstrated by Samadani et al, at least one variable hematoma shape is a predictor for optimal drill location. The expected outcome of this aim is the optimal TDC drill point for maximal drainage based on CSDH radiographic features.

Aim 3. Develop augmented reality for neurosurgical planning for Twist Drill Craniostomy.

(✓) **Aim 3.1. Develop augmented reality for Twist Drill Craniostomy procedure.**

Rationale: In this aim, holograms of the volumetric models will be created using Materialise 3-Matic. The following models will be created-skull, brain, hematoma, and drill point for the Microsoft Hololens⁸⁹.

Approach: The models created with the algorithm mentioned in Aim 1.3 have triangles > 200000, particularly the brain and the skull. The Microsoft hololens cannot render any object with > 200000 triangles due to computational limitations of the hololens first generation hardware⁹¹. The mesh resolution is reduced while keeping the structure intact using the reduce feature in the remesh toolbox in 3-matic⁸⁹. Microsoft Unity v.2019.4.11f1 is used to create the application build needed to deploy the holograms to the hololens⁹¹. **Data Analysis and Interpretation:** 3D objects in Unity can be imported as an .obj or .fbx file format, neither of which store material properties such as color. Material, direction of light in addition to physics properties such as spatial mapping, collision boundaries and interaction need to be added to the holograms with custom C# scripts. The properties can be tested in the scene view in the software during development (Figure 14) ^{91, 92}. We have added the minimum interaction properties needed. We will continue development to include near and far grab interactions important for scaling, voice commands for hologram manipulation and overall improved user experience with augmented reality utilizing the Mixed Reality Toolkit in Unity⁹¹.



Figure 14. Scene View in Unity. The Scene View depicts how the object will be deployed to the hololens.

Material, direction of light in addition to physics properties such as spatial mapping, collision boundaries and interaction need to be added to the holograms with custom C# scripts. The properties can be tested in the scene view in the software during development (Figure 14) ^{91, 92}. We have added the minimum interaction properties needed. We will continue development to include near and far grab interactions important for scaling, voice commands for hologram manipulation and overall improved user experience with augmented reality utilizing the Mixed Reality Toolkit in Unity⁹¹.

(✓) Aim 3.2. Deploy holograms to the Microsoft Hololens.

Rationale: Visual Studio 2019 is used to deploy the application build created with Microsoft Unity in aim 3.1. **Approach:** The current build settings include hololens as the target device, x86 architecture built for modern processors, the recommended D3D build type for best performance by Unity documentation, windows 10 software development kit (SDK) to build and run with USB ^{93, 94}. We were successfully able to deploy a 3D hologram created in aim 3.1 to the Microsoft hololens with these settings (Figure 15). We plan to add holographic remoting to the desktop application to utilize wifi for streaming content to and from the hololens, for easier integration of application in a hospital setting and to enable real time display of 3D holograms and optimal drill point⁹⁵.



Figure 15. Deployed Hologram. The Hologram created in Aim 3.1 was deployed and aligned manually to lab mate Sharada Sridhar.

() Aim 3.3. Align holograms to patient.

Rationale: In this aim, we align the hologram manually to a human anatomy. (Figure 15). **Approach:** Vuforia, a feature detection augmented reality library in Unity will be used to automatically align the hologram to the patient⁹⁶. Vuforia has been utilized by Schneider et al for aligning a segmented 3D model of ventricles from a CT scan to a 3D printed patient anatomy, for augmented reality assisted ventriculostomy⁹⁷. Hololens is not capable of facial recognition⁹¹. Vuforia can be used to add virtual markers to a 3D object model such as a CAD file or an obj file. Vuforia automatically detects the features to add markers that can be used to align the hologram to the corresponding real object⁹⁶. Schneider et al facilitated the virtual feature detection in Vuforia by adding a physical marker to the forehead of the 3D printed head. Once the hologram was registered with this marker, they manually fine-tuned the registration with the hololens controller. The spatial mapping of the perfect registration was saved to create the registration matrix to align other segmented anatomies⁹⁷. We plan to augment this method using open cv in python which is capable of facial recognition⁹⁸. Hololens can be used to take a picture of the patient. Vuforia can add markers to the points detected by open cv as facial features to align the hologram to the patient automatically^{96, 98}. Once the skin layer is aligned, the spatial matrix can be used to align the brain, hematoma, and drill point. The layers will be locked to the patient with spatial anchors, a feature provided by Unity to maintain the hologram in place even when a neurosurgeon shifts gaze⁹³.

Aim 3 Pitfalls and Alternate Strategies: The registration method as proposed may not result in an accurate registration. We will employ the method used by Schneider et al to fine tune the performance of the automatic registration algorithm manually using the controller⁹⁷. The expected outcome of this aim is a bedside augmented reality neurosurgical planning system for TDC.

REFERENCES

1. Michel J-P. *Oxford textbook of geriatric medicine*. Third edition.. ed. Oxford, United Kingdom : Oxford University Press; 2018.
2. Teale EA, Iliffe S, Young JB. Subdural haematoma in the elderly. *BMJ : British Medical Journal*. 2014;348(mar11 11):g1682-g1682. doi:10.1136/bmj.g1682
3. Balser D, Rodgers SD, Johnson B, Shi C, Tabak E, Samadani U. Evolving management of symptomatic chronic subdural hematoma: experience of a single institution and review of the literature. *Neurological research (New York)*. 2013;35(3):233-242. doi:10.1179/1743132813Y.00000000166
4. Baiser D, Farooq S, Mehmood T, Reyes M, Samadani U. Actual and projected incidence rates for chronic subdural hematomas in United States Veterans Administration and civilian populations. *Journal of neurosurgery*. 2015;123(5):1209-1215. doi:10.3171/2014.9.JNS141550
5. Weigel R, Schmiedek P, Krauss JK. Outcome of contemporary surgery for chronic subdural haematoma: evidence based review. *Journal of neurology, neurosurgery and psychiatry*. 2003;74(7):937-943. doi:10.1136/jnnp.74.7.937
6. Fomchenko EI, Gilmore EJ, Matouk CC, Gerrard JL, Sheth KN. Management of Subdural Hematomas: Part II. Surgical Management of Subdural Hematomas. *Curr Treat Options Neurol*. Jul 18 2018;20(8):34. doi:10.1007/s11940-018-0518-1
7. Fomchenko EI, Gilmore EJ, Matouk CC, Gerrard JL, Sheth KN. Management of Subdural Hematomas: Part II. Surgical Management of Subdural Hematomas. *Current Treatment Options in Neurology*. 2018/07/18 2018;20(8):34. doi:10.1007/s11940-018-0518-1
8. Lolli V, Pezzullo M, Delpierre I, Sadeghi N. MDCT imaging of traumatic brain injury. *Br J Radiol*. 2016;89(1061):20150849-20150849. doi:10.1259/bjr.20150849
9. Koliass AG, Chari A, Santarius T, Hutchinson PJ. Chronic subdural haematoma: modern management and emerging therapies. *Nat Rev Neurol*. Oct 2014;10(10):570-8. doi:10.1038/nrneurol.2014.163
10. Stanišić M, Hald J, Rasmussen IA, et al. Volume and densities of chronic subdural haematoma obtained from CT imaging as predictors of postoperative recurrence: a prospective study of 107 operated patients. *Acta neurochirurgica*. 2013;155(2):323-333. doi:10.1007/s00701-012-1565-0
11. Nakaguchi H, Tanishima T, Yoshimasu N. Relationship between drainage catheter location and postoperative recurrence of chronic subdural hematoma after burr-hole irrigation and closed-system drainage. *Journal of neurosurgery*. 2000;93(5):791-795. doi:10.3171/jns.2000.93.5.0791
12. Feghali J, Yang W, Huang J. Updates in Chronic Subdural Hematoma: Epidemiology, Etiology, Pathogenesis, Treatment, and Outcome. *World neurosurgery*. 2020;141:339-345. doi:10.1016/j.wneu.2020.06.140
13. Prevention CfDCA. Facts about Falls. <https://www.cdc.gov/falls/facts.html>
14. Rubenstein LZ, Josephson KR. The epidemiology of falls and syncope. *Clinics in geriatric medicine*. 2002;18(2):141-158. doi:10.1016/S0749-0690(02)00002-2
15. You W, Zhu Y, Wang Y, et al. Prevalence of and risk factors for recurrence of chronic subdural hematoma. *Acta Neurochirurgica*. 05/01 2018;160doi:10.1007/s00701-018-3513-0
16. Adhiyaman V, Asghar M, Ganeshram KN, Bhowmick BK. Chronic subdural haematoma in the elderly. *Postgraduate Medical Journal*. 2002;78(916):71. doi:10.1136/pmj.78.916.71
17. De Bonis P, Trevisi G, de Waure C, et al. Antiplatelet/anticoagulant agents and chronic subdural hematoma in the elderly. *PLoS One*. 2013;8(7):e68732-e68732. doi:10.1371/journal.pone.0068732
18. Biegon A. Considering Biological Sex in Traumatic Brain Injury. *Frontiers in neurology*. 2021;12:576366-576366. doi:10.3389/fneur.2021.576366
19. Peters R. Ageing and the brain. *Postgraduate medical journal*. 2006;82(964):84-88. doi:10.1136/pgmj.2005.036665
20. Gennarelli TA, Thibault LE. Biomechanics of Acute Subdural Hematoma. *The journal of trauma*. 1982;22(8):680-686. doi:10.1097/00005373-198208000-00005
21. Whitfield P, Plaha P, Malhotra D, Heuer D. The management of chronic subdural haematoma. *Advances in clinical neuroscience & rehabilitation*. 2008;8(5):12-15. doi:10.47795/YELG9737
22. Zheng H, Chen C, Zhang J, Hu Z. Mechanism and Therapy of Brain Edema after Intracerebral Hemorrhage. *Cerebrovascular Diseases*. 2016;42(3-4):155-169. doi:10.1159/000445170
23. Shoeb M, Fang MC. Assessing bleeding risk in patients taking anticoagulants. *J Thromb Thrombolysis*. 2013;35(3):312-319. doi:10.1007/s11239-013-0899-7

24. Poon MTC, Rea C, Koliass AG, Brennan PM, British Neurosurgical Trainee Research C. Influence of Antiplatelet and Anticoagulant Drug Use on Outcomes after Chronic Subdural Hematoma Drainage. *Journal of neurotrauma*. 2021;38(8):1177-1184. doi:10.1089/neu.2018.6080
25. Nathan S, Goodarzi Z, Jette N, Gallagher C, Holroyd-Leduc J. Anticoagulant and antiplatelet use in seniors with chronic subdural hematoma: Systematic review. *Neurology*. 04/14 2017;88doi:10.1212/WNL.0000000000003918
26. Motoie R, Karashima S, Otsuji R, et al. Recurrence in 787 Patients with Chronic Subdural Hematoma: Retrospective Cohort Investigation of Associated Factors Including Direct Oral Anticoagulant Use. *World neurosurgery*. 2018;118:e87-e91. doi:10.1016/j.wneu.2018.06.124
27. Motiei-Langroudi R, Alterman RL, Stippler M, et al. Factors influencing the presence of hemiparesis in chronic subdural hematoma. *Journal of neurosurgery*. 2019;131(6):1926-1930. doi:10.3171/2018.8.JNS18579
28. Mehta R, Chinthapalli K. Glasgow coma scale explained. *BMJ*. 2019;365:l1296. doi:10.1136/bmj.l1296
29. Snoey ER, Levitt MA. Delayed diagnosis of subdural hematoma following normal computed tomography scan. *Annals of emergency medicine*. 1994;23(5):1127-1131. doi:10.1016/S0196-0644(94)70115-6
30. Sultan HY, Boyle A, Pereira M, Antoun N, Maimaris C. Application of the Canadian CT head rules in managing minor head injuries in a UK emergency department: implications for the implementation of the NICE guidelines. *Emergency medicine journal : EMJ*. 2004;21(4):420-425. doi:10.1136/emj.2003.011353
31. The future of neurosurgery. <http://lab.neurovascolare.org/2019/02/01/the-future-of-neurosurgery/>
32. SEPS SUBDURAL EVACUATING PORT SYSTEM. <https://www.medtronic.com/us-en/healthcare-professionals/products/neurological/critical-care/seps-subdural-evacuation-port-system.html>
33. Yilmaz H, Boyali O, Atci IB, Kocaman U. Spontaneous resolution of post-traumatic chronic subdural hematoma: a case report. *Pan Afr Med J*. 2017;28:167-167. doi:10.11604/pamj.2017.28.167.13944
34. Kim HC, Ko JH, Yoo DS, Lee S-K. Spontaneous Resolution of Chronic Subdural Hematoma : Close Observation as a Treatment Strategy. *J Korean Neurosurg Soc*. 2016;59(6):628-636. doi:10.3340/jkns.2016.59.6.628
35. Ernestus R-I, Beldzinski P, Lanfermann H, Klug N. Chronic subdural hematoma: Surgical treatment and outcome in 104 patients. *Surgical neurology*. 1997;48(3):220-225. doi:10.1016/S0090-3019(97)80031-6
36. Rahimi-Movaghar V, Rasouli MR, Albright AL. Management of chronic subdural haematoma. *The Lancet (British edition)*. 2010;375(9710):195-195. doi:10.1016/S0140-6736(10)60083-9
37. Kanazawa T, Takahashi S, Minami Y, Jinzaki M, Toda M, Yoshida K. Prediction of postoperative recurrence of chronic subdural hematoma using quantitative volumetric analysis in conjunction with computed tomography texture analysis. *Journal of Clinical Neuroscience*. 2020/02/01/ 2020;72:270-276. doi:<https://doi.org/10.1016/j.jocn.2019.11.019>
38. Vacas S, Cole DJ, Cannesson M. Cognitive Decline Associated With Anesthesia and Surgery in Older Patients. *JAMA*. 2021;326(9):863-864. doi:10.1001/jama.2021.4773
39. Altaf I, Shams S, Vohra AH. Radiological predictors of recurrence of chronic subdural hematoma. *Pak J Med Sci*. Jan-Feb 2018;34(1):194-197. doi:10.12669/pjms.341.13735
40. Golub D, Ashayeri K, Dogra S, Lewis A, Pacione D. Benefits of the Subdural Evacuating Port System (SEPS) Procedure Over Traditional Craniotomy for Subdural Hematoma Evacuation. *Neurohospitalist*. 2020;10(4):257-265. doi:10.1177/1941874420920520
41. Zanaty M, Park BJ, Seaman SC, et al. Predicting Chronic Subdural Hematoma Recurrence and Stroke Outcomes While Withholding Antiplatelet and Anticoagulant Agents. *Frontiers in neurology*. 2020;10:1401-1401. doi:10.3389/fneur.2019.01401
42. Szmuda T, Kierońska S, Słoniewski P, Dzierżanowski J. Modified bedside twist drill craniostomy for evacuation of chronic subdural haematoma. *Wideochir Inne Tech Maloinwazyjne*. 2019;14(3):442-450. doi:10.5114/wiitm.2019.83001
43. Jablawi F, Kweider H, Nikoubashman O, Clusmann H, Schubert GA. Twist Drill Procedure for Chronic Subdural Hematoma Evacuation: An Analysis of Predictors for Treatment Success. *World Neurosurgery*. 2017/04/01/ 2017;100:480-486. doi:<https://doi.org/10.1016/j.wneu.2017.01.037>
44. Silva JNA, Southworth M, Raptis C, Silva J. Emerging Applications of Virtual Reality in Cardiovascular Medicine. *JACC Basic Transl Sci*. 2018;3(3):420-430. doi:10.1016/j.jacbs.2017.11.009
45. Andrews C, Southworth MK, Silva JNA, Silva JR. Extended Reality in Medical Practice. *Curr Treat Options Cardiovasc Med*. Mar 30 2019;21(4):18. doi:10.1007/s11936-019-0722-7
46. Wheeler G, Deng S, Toussaint N, et al. Virtual interaction and visualisation of 3D medical imaging data with VTK and Unity. *Healthcare technology letters*. 2018;5(5):148-153. doi:10.1049/htl.2018.5064

47. Bidgood WD, Jr., Horii SC, Prior FW, Van Syckle DE. Understanding and using DICOM, the data interchange standard for biomedical imaging. *J Am Med Inform Assoc.* May-Jun 1997;4(3):199-212. doi:10.1136/jamia.1997.0040199
48. Varma DR. Managing DICOM images: Tips and tricks for the radiologist. *Indian J Radiol Imaging.* 2012;22(1):4-13. doi:10.4103/0971-3026.95396
49. Dong F, Davros W, Pozzuto J, Reid J. Optimization of Kilovoltage and Tube Current–Exposure Time Product Based on Abdominal Circumference: An Oval Phantom Study for Pediatric Abdominal CT. *AJR American journal of roentgenology.* 09/01 2012;199:670-6. doi:10.2214/AJR.10.6153
50. Hoppe ME, Gandhi D, Stevens GM, Foley WD, Schmidt TG. The effects of gantry tilt on breast dose and image noise in cardiac CT. *Med Phys.* 2013;40(12):121905.
51. Virdee A. Understanding Dicom. 2020. <https://towardsdatascience.com/understanding-dicoms-835cd2e57d0b>
52. *Materialise Reference Guide.*
53. Atlas of human Cardiac Anatomy. <http://www.vhlab.umn.edu/atlas/anatomy-tutorial/anatomic-position.shtml>
54. Multiple Views From CT Scans May Improve Diagnosis. 2005. <https://www.sciencedaily.com/releases/2005/06/050619122405.htm>
55. What is a PACS server? Why do I need one? <http://www.actualmed.com/blog/en/2010/10/20/servidor-pacs-dicom-server/>
56. Darcy Mason s, mrbean-bremen, rhaxton, Jonathan Suever, Vanessasaurus, Dimitri Papadopoulos Orfanos, Guillaume Lemaitre, Aditya Panchal, Alex Rothberg, Markus D. Herrmann, Joan Massich, James Kerns, Koriijn van Golen, Thomas Robitaille, Simon Biggs, moloney, Chris Bridge, Matthew Shun-Shin. pydicom v.2.2.2. <https://doi.org/10.5281/zenodo.5543955>
57. The NIFTI file format. <https://brainder.org/2012/09/23/the-nifti-file-format/>
58. Seo H, Badiei Khuzani M, Vasudevan V, et al. Machine learning techniques for biomedical image segmentation: An overview of technical aspects and introduction to state-of-art applications. *Medical physics (Lancaster).* 2020;47(5):e148-e167. doi:10.1002/mp.13649
59. Alpaydin E. *Introduction to machine learning, third edition.* 3rd . ed. Cambridge, Massachusetts : The MIT Press; 2014.
60. Sangewar S, Peshattiwar AA, Alagdeve V, Balpande R. Liver segmentation of CT scan images using K means algorithm. 2013:6-9.
61. Deng C, Ji X, Rainey C, Zhang J, Lu W. Integrating Machine Learning with Human Knowledge. *iScience.* 2020/11/20/ 2020;23(11):101656. doi:<https://doi.org/10.1016/j.isci.2020.101656>
62. Berka P, Athanasiadis T, Avrithis Y. Rule-based reasoning for semantic image segmentation and interpretation. 2006. p. 39-40.
63. Pape C, Matskevych A, Wolny A, et al. Leveraging Domain Knowledge to Improve Microscopy Image Segmentation With Lifted Multicuts. 10.3389/fcomp.2019.00006. *Frontiers in Computer Science.* 2019;1:6.
64. Xiao C, Chen X, Li W, et al. Automatic Mitochondria Segmentation for EM Data Using a 3D Supervised Convolutional Network. *Methods. Frontiers in Neuroanatomy.* 2018-November-02 2018;12(92)doi:10.3389/fnana.2018.00092
65. Deakyne A. The Uses of Artificial Intelligence and Virtual Reality Platforms for Developing the Next Generation of Anatomical, Medical Device, and Surgical Educational Tools. ProQuest Dissertations Publishing; 2021.
66. Gonzalez RC. *Digital Image processing using MATLAB.* Upper Saddle River, N.J. : Pearson/Prentice Hall; 2004.
67. Monteiro M, Newcombe VFJ, Mathieu F, et al. Multiclass semantic segmentation and quantification of traumatic brain injury lesions on head CT using deep learning: an algorithm development and multicentre validation study. *The Lancet Digital health.* 2020;2(6):e314-e322. doi:10.1016/S2589-7500(20)30085-6
68. Kamnitsas K, Ferrante E, Parisot S, et al. DeepMedic for Brain Tumor Segmentation. Cham: Cham: Springer International Publishing; 2017. p. 138-149.
69. Bhardwaj A. What is Cross Entropy? 2020. <https://towardsdatascience.com/what-is-cross-entropy-3bdb04c13616>
70. Bushaev V. Understanding RMSprop — faster neural network learning. 2018. <https://towardsdatascience.com/understanding-rmsprop-faster-neural-network-learning-62e116fcf29a>
71. Ronneberger O, Fischer P, Brox T. U-Net: Convolutional Networks for Biomedical Image Segmentation. Cham: Cham: Springer International Publishing; 2015. p. 234-241.

72. Jain S, Vyvere TV, Terzopoulos V, et al. Automatic Quantification of Computed Tomography Features in Acute Traumatic Brain Injury. *Journal of neurotrauma*. 2019;36(11):1794-1803. doi:10.1089/neu.2018.6183
73. Rectified Linear Units (ReLU) in Deep Learning. 2017. <https://www.kaggle.com/dansbecker/rectified-linear-units-relu-in-deep-learning>
74. Zhao W, Jiang D, Peña Queraltó J, Westerlund T. MSS U-Net: 3D segmentation of kidneys and tumors from CT images with a multi-scale supervised U-Net. *Informatics in Medicine Unlocked*. 2020/01/01/ 2020;19:100357. doi:<https://doi.org/10.1016/j.imu.2020.100357>
75. Le CT. *Introductory biostatistics*. Second edition / Chap T. Le, Lynn E. Eberly.. ed. Hoboken, New Jersey : Wiley; 2016.
76. Van Rossum G DJF. *Python Reference Manual*. 1995.
77. The Hippa Privacy Rule. U.S. Department of Health and Human Services. <https://www.hhs.gov/hipaa/for-professionals/privacy/index.html>
78. Clustering. <https://scikit-learn.org/stable/modules/clustering.html#k-means>
79. Song Y, Yan H. Image Segmentation Techniques Overview. IEEE;
80. Nécaise RD. *Data structures and algorithms using Python*. Hoboken, N.J. : Wiley; 2011.
81. Fan H. Adaptive marching cubes : a fast 3D surface construction algorithm. M.S. University of Minnesota; 1996.
82. Inserra A, Borro L, Spada M, Frediani S, Secinaro A. Advanced 3D “Modeling” and “Printing” for the Surgical Planning of a Successful Case of Thoraco-Omphalopagus Conjoined Twins Separation. Brief Research Report. *Frontiers in Physiology*. 2020-November-13 2020;11(1427)doi:10.3389/fphys.2020.566766
83. Hughes A, DeBuitléir C, Soden P, et al. 3D Printing Aids Acetabular Reconstruction in Complex Revision Hip Arthroplasty. *Advances in Orthopedics*. 01/10 2017;2017:1-7. doi:10.1155/2017/8925050
84. Xu FF, Chen JH, Leung GK, et al. Quantitative computer tomography analysis of post-operative subdural fluid volume predicts recurrence of chronic subdural haematoma. *Brain Inj*. 2014;28(8):1121-6. doi:10.3109/02699052.2014.910702
85. Humied IA, Abou-Chadi FEZ, Rashad MZ. A new combined technique for automatic contrast enhancement of digital images. *Egyptian Informatics Journal*. 2012/03/01/ 2012;13(1):27-37. doi:<https://doi.org/10.1016/j.eij.2012.01.001>
86. Schetz JA, Fuhs AE. *Fundamentals of fluid mechanics*. New York : John Wiley; 1999.
87. Limkin EJ, Reuzé S, Carré A, et al. The complexity of tumor shape, spiculatedness, correlates with tumor radiomic shape features. *Scientific Reports*. 2019/03/13 2019;9(1):4329. doi:10.1038/s41598-019-40437-5
88. Byrd BK, Krishnaswamy V, Gui J, et al. The shape of breast cancer. *Breast Cancer Research and Treatment*. 2020-09-01 2020;183(2):403-410. doi:10.1007/s10549-020-05780-6
89. 3-Matic Reference Guide. https://s3.amazonaws.com/helpjuice-static/helpjuice_production%2Fuploads%2Fupload%2Fimage%2F5908%2Fdirect%2F1578074370812-3-matic+14.0+--+User+Manual.pdf
90. Bakshi C. Random Forest Regression. <https://builtin.com/data-science/random-forest-algorithm>
91. Glover J, Linowes J. *Complete Virtual Reality and Augmented Reality Development with Unity*. 2019.
92. Unity Development for HoloLens. <https://docs.microsoft.com/en-us/windows/mixed-reality/develop/unity/unity-development-overview?tabs=arr%2CD365%2Ch2>
93. Unity Documentation. <https://docs.unity3d.com/Manual/windowsstore-buildsettings.html>
94. Build and Deploy to HoloLens. Microsoft. <https://docs.microsoft.com/en-us/windows/mixed-reality/develop/unity/build-and-deploy-to-hololens>
95. Holographic Remoting Overview <https://docs.microsoft.com/en-us/windows/mixed-reality/develop/advanced-concepts/holographic-remoting-overview>
96. Frantz T, Jansen B, Duerinck J, Vandemeulebroucke J. Augmenting Microsoft's HoloLens with vuforia tracking for neuronavigation. *Healthcare technology letters*. 2018;5(5):221-225. doi:10.1049/htl.2018.5079
97. Schneider M, Kunz C, Pal'a A, Wirtz CR, Mathis-Ullrich F, Hlaváč M. Augmented reality–assisted ventriculostomy. *Neurosurgical focus*. 2021;50(1):1-7. doi:10.3171/2020.10.FOCUS20779
98. G.Bradski. The OpenCV Library. *DrDobb's Journal of Software Tools* 2000;